A WAAM benchmark: From process parameters to thermal effects on weld pool shape, microstructure and residual stresses

Camille Cambon, Issam Bendaoud, Sébastien Rouquette, Fabien Soulié

A WAAM benchmark: from process parameters to thermal effects on weld pool shape, microstructure and residual stresses.

Camille Cambon, Issam Bendaoud, Sébastien Rouquette* and Fabien Soulié

LMGC, Univ. Montpellier, CNRS, Montpellier, France

Keywords:
WAAM benchmark
GMAW-CMT
in-situ measures
residual stresses
neutron diffraction

ABSTRACT

A two-dimensional experimental setup has been designed to investigate the influence of process parameters during WAAM operation. This experimental study has been also designed as a WAAM benchmark for numerical investigations such as thermal-mechanical ones. Indeed, several measurements have been done in-situ such as welding current and voltage, temperature, weld pool images and local displacement. Some measurements have been realized ex-situ: micro-structure and residual stresses. Residual stresses were investigated by neutron diffraction technique on two specimens. The experiments consisted in the deposition of 5 successive layers of 316L stainless steel filler-wire. 3 sets of process parameters were investigated based on variations of travel speed and linear energy from 147.1 to 189.7 J/mm. The welding thermal cycle was clearly visible on the time evolution of the displacement, also varying cyclically by a few tenths of a millimeter, as well as on the weld pool size. The weld pool size increased (up to 5 mm) with the number of layer increasing as the initial temperature of the specimen was higher due to the previous deposited layer. The micro-structure is textured with columnar dendrites of few millimeter long. The effect of studied process parameters on the residual stresses is slightly perceptible in the melted zone.

1. Introduction

Wire + arc additive manufacturing (WAAM) process is based on layer-by-layer deposition of melted filler-wire. This process uses an arc welding source to provide the heat required to melt both the metallic parent and filler-wire (Jin, Zhang, Jin, Tian, Wellmann and Liu, 2020; Henckell, Gierth, Ali, Reimann and Bergmann, 2020; Tabernero, Paskual, Álvarez and Suárez, 2018). Additive manufacturing processes are an interesting alternative to traditional substractive processes to produce components with less waste of raw materials (Williams, Martina, Addison, Ding, Pardal and Colegrove, 2015). WAAM has higher deposition rate than additive manufacturing processes using metallic powders as well as its costs are lowered thanks to the use of welding sources (Ding, Pan, Cuiuri and Li, 2015). However, as observed in welded parts, WAAM process can result in distortions and residual stresses in the manufactured components that can directly affect their fatigue behavior (Michaleris and Debiccari, 1997; Colegrove, Coules, Fairman, Martina, Kashoob, Mamash and Cozzolino, 2013; Colegrove, Ikeagu, Thistlethwaite, Williams, Nagy, Suder, Steuwer and Pirling, 2009). These distorsions and residual stresses are mainly due to the deposition thermal cycle (so the process parameters) and deposition strategy: scan path and dwell time Jin et al. (2020). Distortions and residual stresses of WAAM parts have been studied with the help of thermo-mechanical simulation (Ding, Colegrove, Mehnen, Ganguly, Almeida, Wang and Williams, 2011; Wu, Mukherjee, De and DebRoy, 2020). Some studies were completed with stress measurements on the WAAM parts Ding et al. (2011); Honnige, Williams and Roy (2017).

There is a growing number of studies reporting both numerical and experimental results, including layer deposition strategy (number of layers, dwell time), temperature measurement and post-mortem residual stresses measurements (Sun, Hensel, Köhler and Dilger, 2021; Abusalma, Eisazadeh, Hejripour, Bunn and Aidun, 2022). However, there is no much more benchmark dedicated to the WAAM operation that provides in-process data (electric signals, temperature, weld pool images and distortions) and post-process data (micro-structure and residual stresses) according to different set of process parameters (or welding linear energies). The main objective of this work is to evaluate the effects of process parameters, that is to say: welding voltage and current as well as the travel speed reported as linear energy, on the distortions and residual stresses of manufactured parts. This experimental study is also designed as a benchmark and could be used for further comparisons and discussions with numerical simulation

*Corresponding author
sebastien.rouquette@umontpellier.fr (S. Rouquette)
ORCID(s): 0000-0002-1849-6142 (S. Rouquette); 0000-0002-7592-2312 (F. Soulié)

such as thermal-metallurgical or thermal-mechanical ones. The proposed experiments provide then local thermal information (temperature measurement, weld pool geometry) and mechanical information (local displacement) during deposition for 3 sets of process parameters. These informations are completed by a posteriori cross-section observations (macrography and EBSD analysis) and residual stress measurements. With this idea of being used as a relatively complete benchmark, the experimental configuration is two-dimensional, thus, under plane stress assumption, what simplifies the subsequent implementation of numerical simulation.

First, a general overview of the setup is given with a description of samples, measurements and settings. The next parts present the experimental results obtained for weld pool, temperatures, displacements during the deposition of the layers. One section is dedicated to the residual stresses measured by neutron diffraction technique for two samples. The results are discussed in relation with the process parameters in the last section.

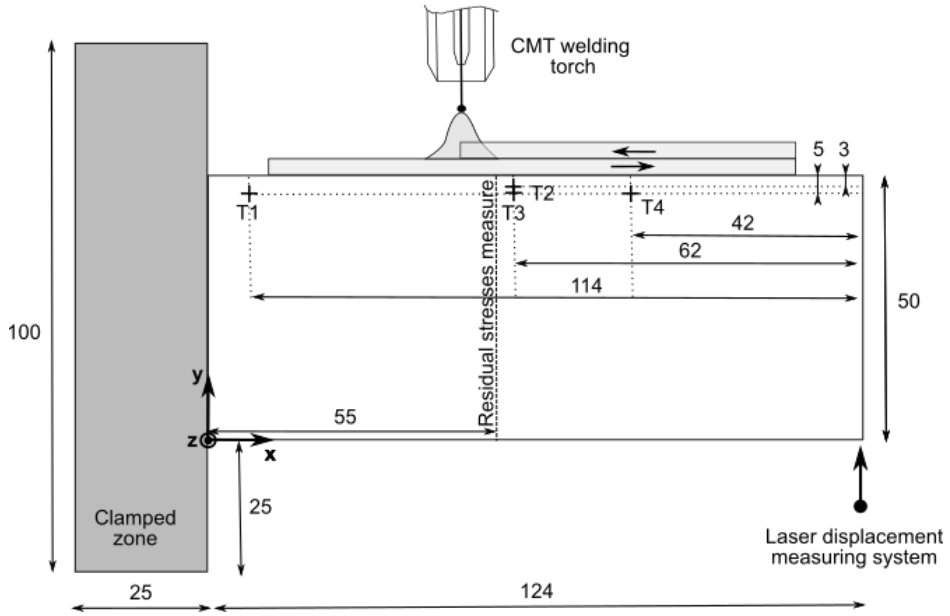

Figure 1: Configuration of the experimental sample with the dedicated instrumentation. The grey zone corresponds to the clamping zone. The dimensions are expressed in mm, and the cross-symbols with 'T' references indicate K-type thermocouple locations. Another thermocouple, referred as T5, is located on the other side of the sample, symmetrically to T3 (see table 2 for additional information). The vertical dashed line corresponds to the line where residual stresses have been measured. The dotted arrow corresponds to the location of the displacement measuring system. The origin of the z-axis is in the plane of symmetry of the sample (half thickness).

1.1. Experimental setup

The experimental setup consisted in depositing the melted metallic filler-wire on the thickness of a base plate held vertically, along the longitudinal direction such as depicted in figure 1. This setup is chosen to be comparable to a 2D plane stress condition as the thickness (6 mm) is smaller than the two other dimensions (149 x 50 mm) Cambon, Rouquette, Bendaoud, Bordreuil, Wimpory and Soulié (2020). The size of the base plate and the deposits are also defined according to this criteria. The area of the deposit zone of the base plate is 124 mm by 6 mm. The base plate is clamped on its massive left side and free on the other ones. The metal deposition is realized on its top, see figure 1. The considered filler material is 316L Stainless Steel. Up to five layers are deposited alternately such as the starting point of the next layer is the ending point of the previous one. The cooling time (or dwell time) between each layer is about 35 s. The deposit length is 100 mm and its average height is about 2 mm per layer.

The Cold Metal Transfer (CMT, Fronius) have been used as heat source for melting the metallic filler-wire and base plate. The CMT is a specific controlled short-circuit Gas Metal Arc Welding. The main characteristic of this process is its ability to control forth and back the wire feeding. The CMT process directly controls the wire feed speed (S_f) and the heat input UI (welding current I and arc-voltage U, see figure 2), whereas the motion of the welding torch is performed with a 6-axis robotic arm (Kuka KR 16) controlling the trajectories and the travel speed (S_w or

Table 1
Process parameters used in the experiments. For each set of parameter (tagged #Si), a set of values is defined for the first layer (tagged #$SiL1$) and another set is defined for the additional layers (tagged #$SiLn$).

Parameters	**Set** 1 **layer** 1	**Set** 1 **layer** n	**Set** 2 **layer** 1	**Set** 2 **layer** n	**Set** 3 **layer** 1	**Set** 3 **layer** n
U (V)	13.5	13	14.5	13.6	14.5	13.6
I (A)	119	99	144	122	144	122
S_w (m/s)	0.007	0.007	0.007	0.007	0.0086	0.0086
E (J/mm)	183.6	147.1	238.7	189.7	194.2	154.3
S_f (m/min)	3.2	2.5	4.2	3.3	4.2	3.3

Table 2
Position of thermocouples reported in the (x, y, z) coordinate system of figure 1 (z =0 mm is on the symmetry plane).

Thermocouple number	**T**1	**T**2	**T**3	**T**4	**T**5
position on the longitudinal x-axis (mm)	10	62	62	82	62
position on the transverse y-axis (mm)	45	47	45	45	45
position on the normal z-axis (mm)	2	2	2	2	-2

welding speed). The travel speed affects the rate of heat input to the deposit zone and then the mechanical state of the manufactured part. Consequently, the study will take into account the effect of welding parameters as the heat input per unit length of weld. This parameter is defined as the linear energy $E = \frac{UI}{S_w}$.

1.2. Settings

The shielding gas is a binary mixture: 98% Argon and 2% CO_2. The stick-out is set to 10 mm and checked before each deposition with the help of a gauge block. The metal deposit is a 316L stainless steel wire of 1.2 mm diameter. Three sets of process parameters were used in order to study the influence of the process parameters on the thermal cycle and residual stresses. These process parameters are summarized in table 1. #$S1$ was referred as nominal set of parameters according to the desired geometry of deposit, #$S2$ was used to obtain an higher linear energy with a same welding speed, whereas #$S3$ was chosen to appreciate the influence of welding speed with a similar linear energy as #$S1$. For each set of parameter (tagged #Si), a specific setting was applied for the first layer (tagged #$SiL1$) in order to guarantee a good heating of base plate and good quality of the weld bead for the deposition of the additional layers. The three sets of parameters were applied from the second layer (tagged #$SiLn$). Let's notice that the welding current I and arc-voltage U were time-averaged on the base of the recorded electrical waveforms as shown in figure 2.

1.3. Measures

Temperature measurements, weld pool images and local displacement of free end corner of the specimen were recorded in-situ in order to investigate the effect of process parameters. Some complementary post-process analysis were carried out such as macrographic analysis and stress measurements.

1.3.1. In-situ measures

Welding current and arc voltage, temperature, displacement, video of weld pool were monitored with a synchronized data acquisition during the WAAM operation. Welding current and arc voltage were recorded at 30 kHz sampling rate (figure 2) during the first and second layer deposits. The calculation of the linear energy supplied to the system was based on these measurements.

Temperatures were locally measured within the base plate and close to the deposition zone (see figure 1) with type-K thermocouples of 0.5 mm diameter. Four thermocouples were located on one side of the base plate and another one was located on the other side, symmetrically to the central plane. The positions are reported in figure 1 as well as in table 2. The recording lasted 2500 s with a 20 Hz sampling rate in order to get the complete thermal cycle (heating and cooling stages).

The weld pool was recorded during short-circuit periods using a CCD camera. A narrow-band filter was placed on camera lens in order to cancel the brightness of electric arc Monier, Thumerel, Chapuis, Gilles, Soulié and Bordreuil

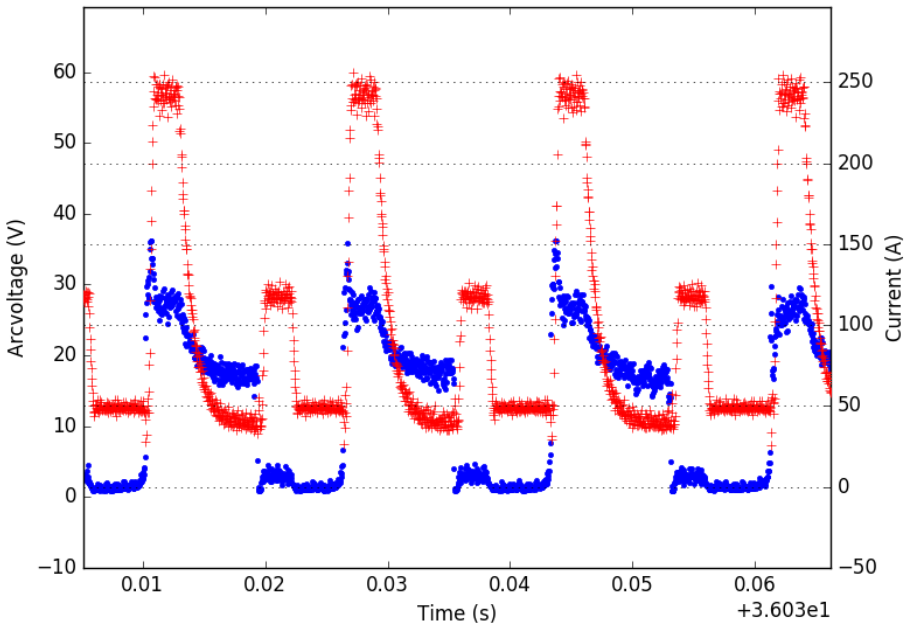

Figure 2: Typical electrical waveforms (arc-voltage, in blue dots, and welding current, in red '+') monitored during a deposit operation with CMT process. The short-circuit periods are typical of CMT process.

(2016). These two techniques allowed recording the weld pool when the arc is off (during the short-circuit time). The camera was installed on the lateral side of the welding torch in order to record the weld pool. The pictures have been used for determining the weld pool size and for post-process visualization. The displacement of the base plate was measured with a laser system (Micro-epsilon scancontrol 2600) located at the lower free part of the base plate as shown in figure 1. The measurement have been done every 5 s during 800 s from the beginning of the experiment, including the heating and cooling cycles.

1.3.2. Post-process measures

Macrographic analysis have been realized as multiple specimens were fabricated under the same process conditions. Some specimens were used to check the quality of the deposits (e.g. lack of porosities) and for visualizing the different deposited layers.

2. Results

In this section, only the #$S1$ results are presented and discussed for simplifying the understanding of the WAAM process.

2.1. Melted pool and fusion zone

Figure 3 shows the weld pool images at different steps of the deposition. The melted pool is presented for the first and second layers. The first column of images shows the weld pool initiation on the thickness of the base plate, initially at room temperature (293 K), and the very beginning of the first layer deposit. The images of the second column present the first layer deposit, with a motion of the welding torch from the right to the left. The weld pool has grown in the first stages and then its shape stabilized that showed a thermal steady state was reached for this layer. The third and last column presents the initiation and the deposit of the second layer, with an alternate direction of deposit, the welding torch moving from the left to the right of the pictures.

The shape and size of the weld pool have been extracted after images processing. From these weld pool images, the average length of the weld pool was evaluated to 15.0 ± 0.4 mm for the first layer then to 18.5 ± 0.3 mm for the third

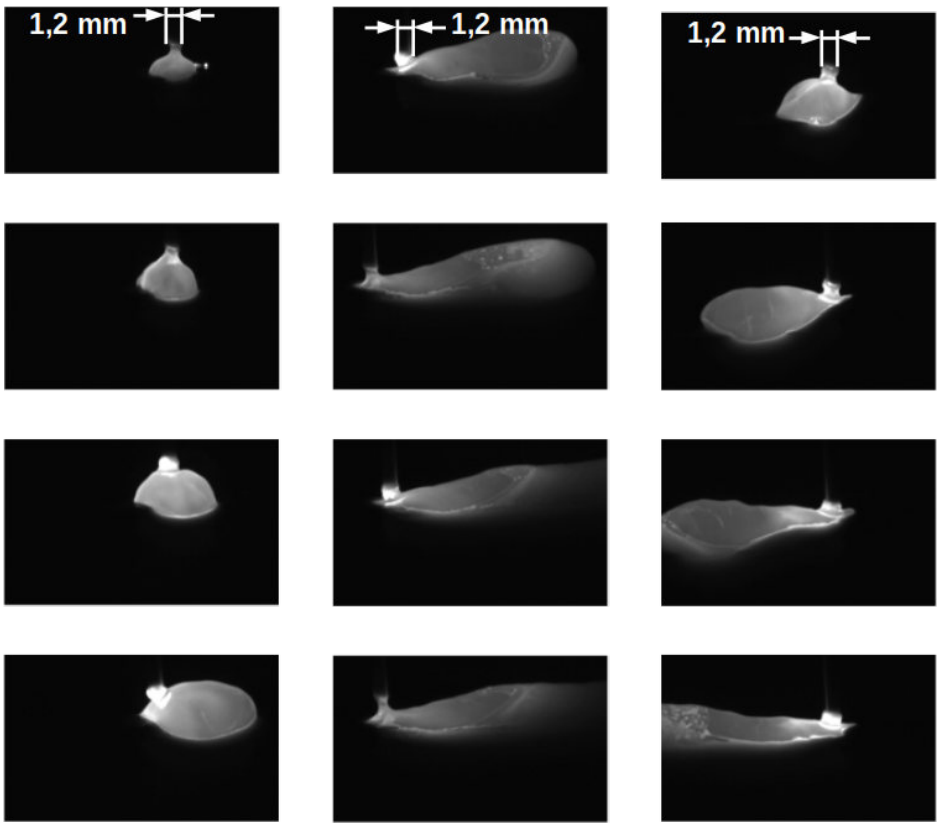

Figure 3: Images obtained with the camera located on the side of the welding torch during the deposit of melted wire: initiation of weld pool for the first layer (1st column), during the 1st layer (2nd column) and for the 2nd layer (3rd column). Experiment was realized with #$S1$ set of parameters (for dimension indication, the diameter of the feed wire is 1.2 mm).

layer and to 19.5 $\pm$ 0.4 mm for the fifth layer. Despite a higher linear energy used for the deposition of the first layer (see Table 1), the observed weld pool was smaller than the one recorded for layers 3 and 5. The effect is due to the heat sink effect of the base plate. Indeed, the first layer was deposited on a "cold" base plate with an initial temperature of 293 K. The next layer was realized 35 s after the previous one was finished. The dwell time of 35 s was not enough to let the specimen cooling down to the room temperature so the initial temperature of the specimen for layers 2, 3, 4 or 5 were 200-300 K higher than the room temperature. This temperature increase of the whole specimen after each deposited layer led to large weld pool size. This is clearly visible in figure 6 at 60 s, 110 s, 161 s and 211 s that are the starting times of layers 2, 3, 4 or 5 respectively. The increase was most important between layer 1 and layer 2 with 260 K while the increase was about 60 K between layer 2 and 3. Let's notice that the thermal steady state was achieved within each layer, nevertheless, the addition of a new layer led to warmer conditions and larger weld pool sizes.

Figure 4 presents macrographic views of the cross-section localized at 52 mm and 86 mm from the beginning of the 5 layers specimen. The first one, localized in the center part of the sample, corresponds to a stationary regime area. Five different layers are noticed and, thus, the corresponding solidus lines. No defects such as porosities have been observed. The (re)fusion of the previous deposited layer is clearly visible that underlines the quite good quality of the process. In the center part (figure 4(a)), the global height of the deposited sample is about 10 mm whereas it is about 9.8 mm near the extremity (figure 4(b)). It corresponds to an approximate 2 mm height for each layer. In the stationary regime area, the geometrical measurements of base plate and fusion zones allows measuring the weld pool penetration for the first layer (along the vertical longitudinal plane of symmetry). The observed penetration of the fusion zone is about 1.5 mm in this area, corresponding to the position of the liquidus during the welding process.

These macrographic views provided informations on the microstructure of the fusion zone, confirmed by the EBSD shown in figure 5. The structure is mainly columnar dendritic with an epitaxial growth on different layers. An equiaxed dendritic zone is noticeable in the central part of the first layer. It could correspond to an equiaxed to columnar transition

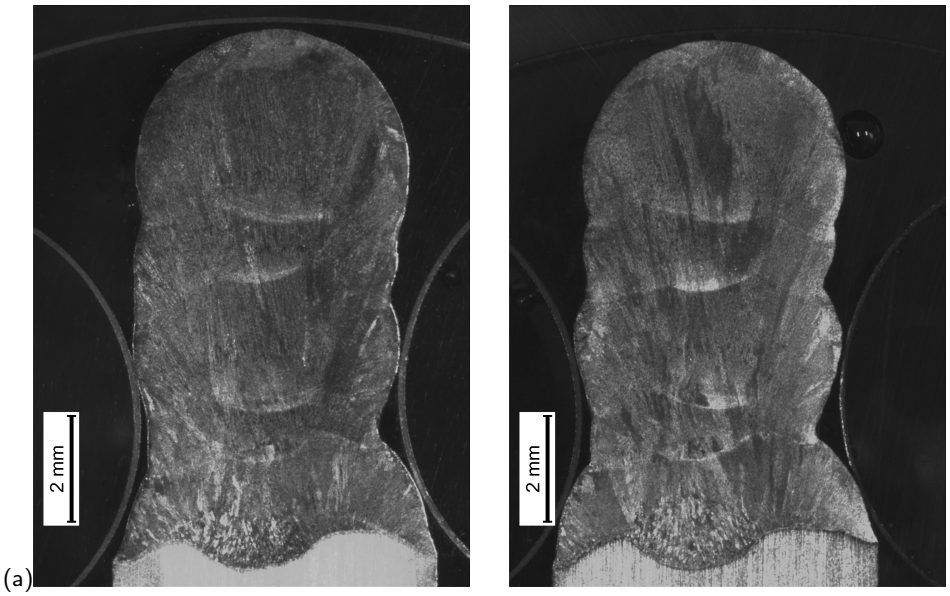

Figure 4: Macrographic view of 5 layers specimen obtained with #$S1$ set of parameters. The cross-section is localized at (a) 52 mm and (b) 86 mm from the beginning of the deposited wall. The base plate, corresponding to base material, is 6 mm in thickness.

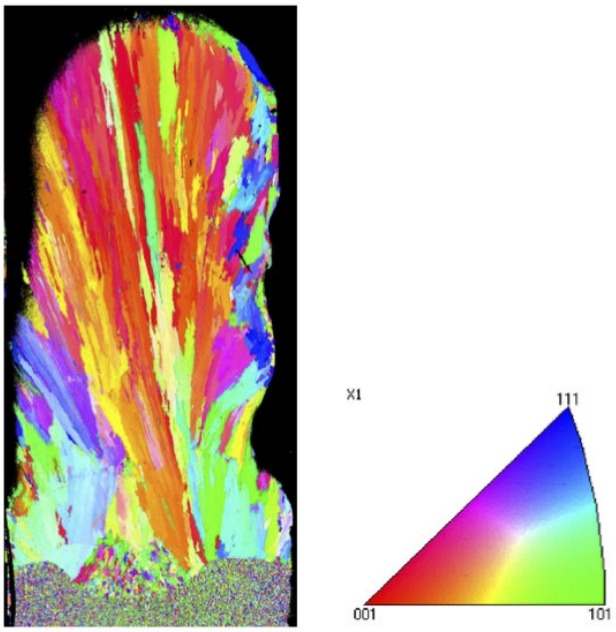

Figure 5: EBSD of the middle section of deposit sample obtained with #$S1$ set of parameters.

zone often observed in the central part of weld pool due to the evolution of the ratio between temperature gradient and growth rate Kou (2003). The wavy form of the fusion line (between base plate and first layer) is likely due to the combined effects of fluid motion in the weld pool, see figure 4, surface tension effect that maintains the liquid metal and the geometry of the base plate.

2.2. Temperatures

Figure 6 presents the thermal cycles measured with K-type thermocouples inserted in the base plate. Their positions are reported in figure 1 and in table 2. This thermal cycles were obtained with #$S1$ set of process parameters. The 5 thermocouples were inserted in 1 mm diameter holes drilled into the base plate then bonded to it with special hot temperature paste. The five thermal cycles corresponding to the five deposited layers are well observed. The highest temperatures were obtained with thermocouple T2 which was the closest to the deposit zone. Thermocouple T2 was situated 3 mm underneath the 1st layer. The cooling cycles are similar to the ones observed during a welding operation Poorhaydari, Patchett and Ivey (2005). The different thermal cycles converged to the room temperature around 1800 s as it is reported in table 3. The cooling rates for thermocouples T2, T3, T4 and T5 are identical. The global thermal cycles obtained for thermocouples T3 and T5 are very close, both during deposition and cooling periods as shown in figure 6 and also in table 3. This trend was expected as these two sensors were facing each other according to the symmetrical plane xy see figure 1. Moreover this trend confirmed the repeatability and reliability of measurement technique.

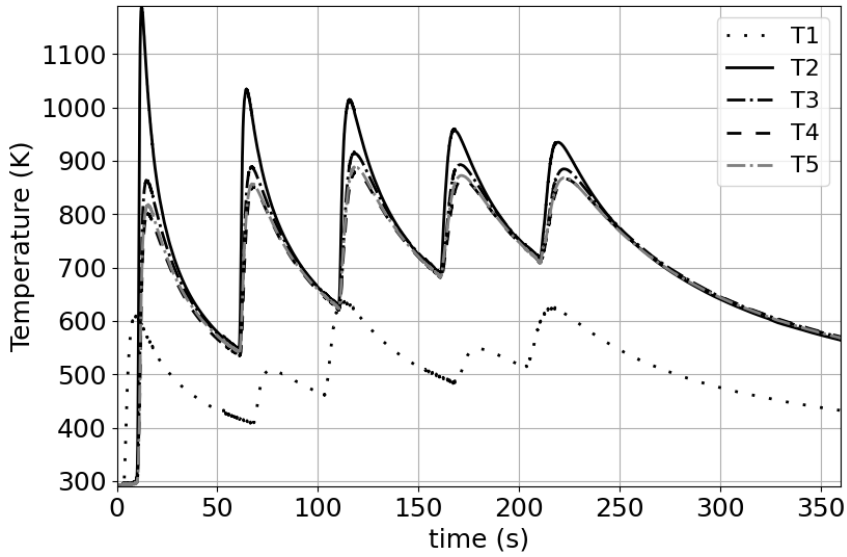

Figure 6: Thermal cycles obtained during the WAAM deposition and the cooling periods for #$S1$ set of parameters. The thermocouples are identified according to their locations defined in figure 1.

The position of the thermocouples emphasizes the alternative deposition strategy through the magnitude and the temporal occurence of the temperature peaks. This is clearly noticeable for T1, and, to a lesser extent, for T4. The differences in maximal temperature between odd and even layers of T1 are due to the location of the thermocouple at the start (odd layer) or end (even layer) of the deposits. For the odd layers, this location corresponds to the start of the layer with a stationary position of the welding torch during the initiation of the electrical arc and development of the weld pool. Then its temperature peak is quickly reached followed with a long cooling time: 90 mm of deposition time $\sim$12.8 s at welding speed of 7 mm/s (for ending the deposit as the torch moves away) plus a 35 s dwell time between each layer. As a consequence, this zone of the base plate had a long time to cool down. For the even layers, thermocouple T1 corresponds to the end of the layer with a rapid extinction of the arc plus 35 s of dwell time. Finally, the odd layer has a cooling time 24 s longer than for an even layer. This explains the observed difference for thermal cycle 1 and 2: cooling time of thermal cycle 1 is almost twice longer than thermal cycle 2. The cooling time of thermal cycle 2 is slightly longer than the break time of 35 s. The temperature peak of heating cycle 2 is lower than the temperature peak of heating cycle 1. There are two causes: first, the thermocouple position led to longer cooling time and, secondly, each deposit resulted in an increase of almost 2 mm of the depth from the top surface. The 3rd heating cycle led to an higher temperature for T1 for two reasons : the 2nd cooling time is shorter and the arc welding arc is initiated above T1 (new odd layer). Thermocouple T4 is subject to the same effect of T1 as it is located 30 mm before the end of the

Table 3
Evolution of the temperature as a function of time for thermocouples T2, T3, T4 and T5 until 1800s.

Thermocouple	**12.5 s**	**64.5 s**	**115.5 s**	**168 s**	**220 s**	**250 s**
T2 (K)	1189	1034	1013	958	934	773
T3 (K)	747	843	886	882	879	774
T4 (K)	662	773	846	841	856	770
T5 (K)	689	807	856	858	862	768
Thermocouple	**300 s**	**400 s**	**600 s**	**800 s**	**1200 s**	**1800 s**
T2 (K)	641	532	444	397	346.8	316.8
T3 (K)	645	536	447	398.4	347.6	317.1
T4 (K)	646	538	450	401	349.5	317.8
T5 (K)	644	535	446	398.3	347.8	317.1

deposit. During the odd layer (e.g. 1st layer), its cooling time is shorter than the one of the even layer (e.g. 2nd layer). Conversely to T1, its temperature peaks did not decrease between each layer probably for two reasons: on one hand, the difference in cooling time between odd and even layers is not enough long and, on the other hand, thermocouple T4 is close to the base plate end, surrounded with the air atmosphere, where the heat is likely accumulated. Conversely to thermocouple T1, the heat was likely transferred to the clamping system.

Thermocouple T2 is located 3 mm underneath the surface (for the 1st thermal cycle) at mid distance from each ends of the deposit, the maximum temperature reached 1189 K for the 1st thermal cycle then the temperature peaks decreased as the number of deposited layers increased because its depth from the top surface has risen of almost 2 mm at each added layer. This is mainly due to thermal conduction and heat losses effects. There is no differences in cooling time due to odd and even layer effect. The temperature decrease for T2 is due to combined effect of the addition of matter and decrease of linear energy between the first layer and layers 2 to 5 according to table 1. For thermocouples T3, T4 and T5, the measured peak temperatures stabilized after the third layer; approximately around 858 K - 882 K for T3 and T5 and around 841 - 856 K for T4. Moreover, the values reported in table 3 underlines fairly good agreement between T3 and T5 for the whole thermal cycles which confirms their symmetrical location.

The initial temperature has increased at the beginning of each deposited layer due to the accumulated thermal effect of the previous cycle. This increase is observed at all thermocouples whatever their location. The thermal loading occurring layer after layer led to an overall accumulation of heat in the substrate. As a matter of fact the temperature at the end of the cooling cycle is greater than the one at the beginning of the heating cycle. That global thermal increase contributed to longer weld pool for the last deposited layer. The uncertainties on the temperature are relatively low (about 5%) what exhibits a good repeatability of the thermocouple measurements. The highest standard deviation is localized at the temperatures peaks where the heating rate is high and quickly turn down to cooling. The uncertainties on temperature measurements were estimated statistically by calculating the average temperature over all the experiments carried oud under the same operating conditions. The experiments were repeated up to 6 times for a same set of linear energy.

2.3. Global displacement

The vertical displacement was recorded with a laser system located under the right free end of the base plate as defined by the dotted arrow in figure 1.

The largest section of the substrate was clamped firmly in a vice. The free section of the substrate, upon which the layer is deposited, is supposed to behave as a cantilevered beam. The laser displacement device did not measure any lateral displacement of the substrate what confirmed the plane stress assumption. The measured displacements represent the variations of substrate bending. These variations of bending report a global deformation of the substrate.

The measured displacements up to five deposited layers are presented in figure 7 for set $\#S1$ of process parameters. The value zero corresponds to the reference position of the substrate free end before the deposition procedure started. The positive values (or rising cycle of the curve) is related to an upward displacement while negative values (or dropping cycle of the curve) represent a downward displacement of the substrate. For each layer, the deposition procedure was characteristic of a high heating and addition of melted metal then followed of 35 s cooling cycle (or dwell time). The high heating (from the electric arc) caused a thermal expansion of the upper longitudinal zone of the substrate

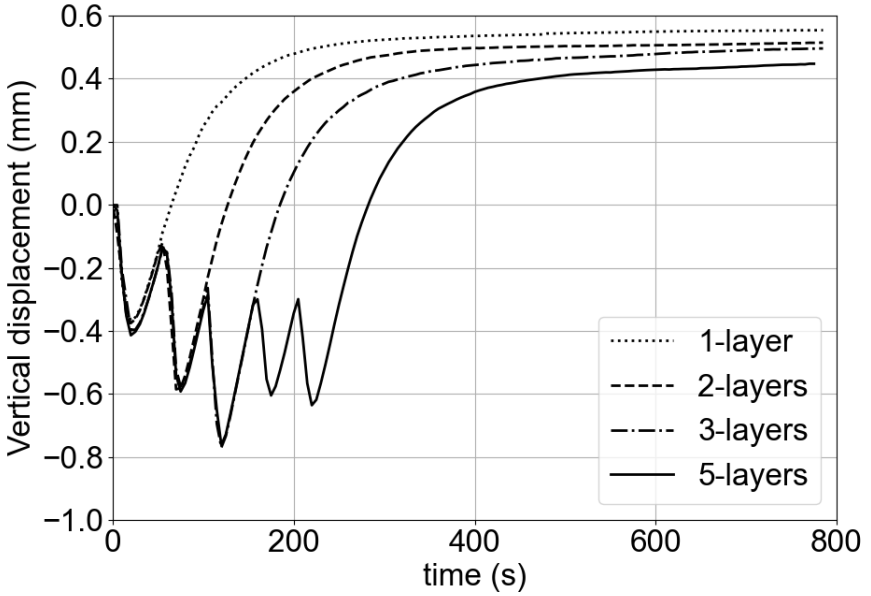

Figure 7: Vertical displacements measured during the deposition of one to five layers with #$S1$ sets of process parameters. The displacement is recorded with a laser displacement device located at the right bottom part of the sample as defined by the dotted arrow in figure 1.

and, thus, a downward displacement of substrate free end. During the cooling cycle, the upper longitudinal zone shrank causing an upward displacement of the substrate free end. Each deposited layer is described with a downward – upward displacement because of the heating and cooling cycles as it is reported in figure 8.

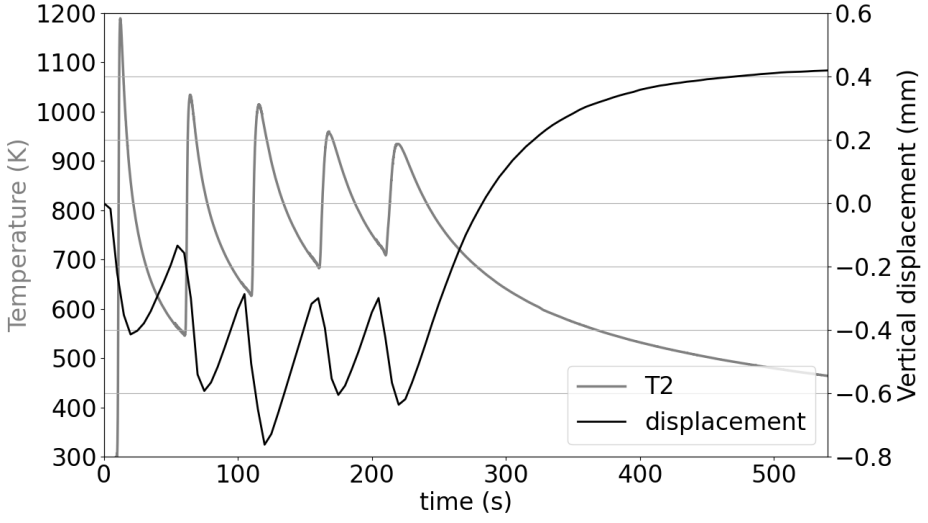

Figure 8: Vertical displacement and T2 temperature measured during the deposition of five layers with #$S1$ sets of process parameters. (T2 position is presented in figure 1).

The last cooling cycle is characterized by a largest upward displacement because the whole substrate was cooling down to room temperature. An inflexion point in the upward displacement is observed 120 s after the start of last cooling

Table 4
Final vertical displacement of each specimen built under set #$S1$. The uncertainty on the vertical displacement is estimated to ± 0.03 mm.

	1-layer	2-layers	3-layers	5-layers
Disp. (mm)	0.55	0.51	0.48	0.44

Table 5
Main neutron diffraction settings used (GV means Gauge Volume in mm^3).

Place	Crystal plane	Wave-length	2θ angle	GV-long	GV-trans	GV-norm
HZB	Fe-311	1.471∀	85.584°	2x2x2	2x2x2	10x2x2
ILL	Fe-311	1.66∀	98.502°	2x0.6x2	2x0.6x2	2x0.6x2

cycle. The final displacement of the substrate free end is around +0.44 mm for the 5-layers specimen. The overall shape of the specimen corresponds to a longitudinal bending due to the thermal shrinkage of its upper section in addition to the cantilever effect (the left side of the substrate is clamped and the right one is free to move as presented in figure 1). No displacement was observed along the z axis (through the thickness), confirming the plane stress assumption for the studied configuration.

The largest vertical displacement is observed with the 1-layer specimen, about 0.55 mm, and decreased steadily to 0.44 mm with the 5-layers specimen. The trend is clearly observed from 1-layer to 5-layers as reported in figure 8 and in table 4. The downward - upward displacement stabilized after the third deposited layer. This trend was observed on the temperature at the beginning of each layer which stabilized after the 3rd layer, figure 6. The initial temperature before the 4th and 5th layer was about 700 K. That means that the thermal gradient between the melted zone and inside the specimen is lower than the one produced during the deposition of three first layers. Indeed, the highest thermal gradient was reached for with the 1-layer specimen and it ended with the largest vertical displacement. It is likely that the vertical displacement achieved with the 5-layers specimen is a sort of asymptotic limit. The minimum downward displacement is reached at the end of the deposition of the 3rd layer. The thermal cycles produced during the 4th and 5th layer led to similar downward and upward displacements. That likely traduced that layers 4 and 5 had a similar thermal cycle and the addition of a new layer should be similar to the one of layers 4 and 5 (if the dwell time is not modified).

2.4. Residual stresses

The different neutron diffraction settings used at the ILL and HZB facilities are reported in table 5. Measurements were made along three directions: the longitudinal direction (LD) parallel to the layer, the transverse direction (TD) (or y direction according to figure 1) and the normal direction (ND) is perpendicular to the surface of the plate (or z direction). The normal and longitudinal directions were measured without unmounting the specimen. For the measurement of the transverse direction, the specimen was rotated of 90°. However, given that the thickness of the deposit was less than 6 mm (smaller than the size of parent : 149 mm by 50 mm and 6 mm thick), plane stress in the XY-plane was assumed, see 1. Then it was possible to deduce the unstrained lattice parameter (d_0), and thus $2\theta_0$, from the three measurements of 2θ diffracted angles. This assumption imposes that the normal stress was assumed equal to zero ($\sigma_{normal} = 0$) Hutchings, Withers, Holden and Lorentzen (2005); Akrivos, Wimpory, Hofmann, Stewart, Muransky, Smith and Bouchard (2020); Martina, Roy, Szost, Terzi, Colegrove, Williams, Withers, Meyer and Hofmann (2016). The uncertainty on the stress values at each location was determined using a propagation of uncertainty approach, taking into consideration the uncertainty of the $2\theta_0$ calculation, the uncertainty of 2θ measurement and the uncertainty of the strain calculation according to Hooke's law Wang, Denlinger, Michaleris, Stoica, Ma and Beese (2017).

Figures 9 and 10 present respectively the longitudinal and transverse stresses along the vertical dashed line displayed in figure 1. The specimen analyzed at HZB was manufactured with #$S1$ set of process parameters while the second specimen, sent to the ILL, was made with #$S2$ (thus higher welding energy, see table 1). The two longitudinal stress distributions are fairly similar for both specimens. The deposition zone is situated beyond 53 mm on the y vertical axis. The highest stress peak was measured nearby the parent - deposits interface, at 53 mm, with a value around 220 MPa. This zone was subjected to high thermal gradients especially during the first thermal cycle as the

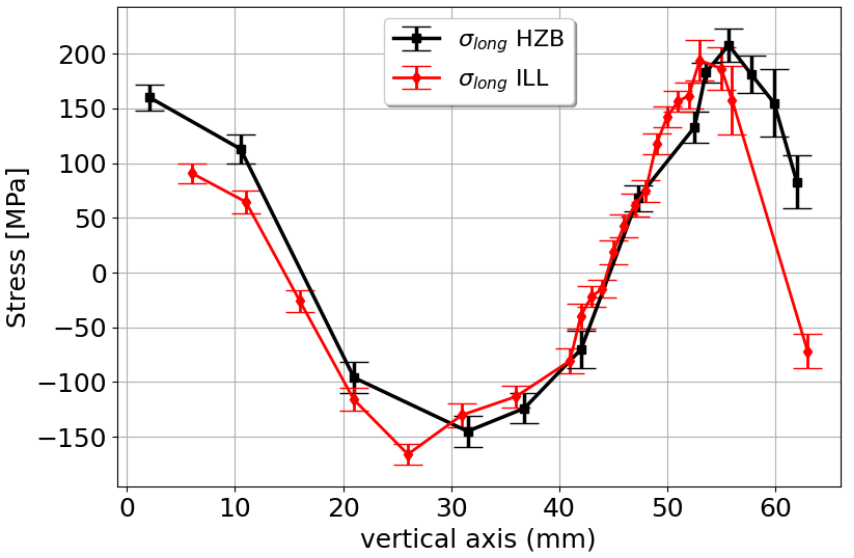

Figure 9: Longitudinal stress distributions along a vertical line located at x = 55 mm for two different specimens: the specimen identified HZB was built under settings 1 while the one identified as ILL was made under settings 2 (with a standard deviation of two sigma). The residual stresses in the specimen 1 were measured at Helmholtz Zentrum of Berlin (Germany) Cambon et al. (2020). The residual stresses in specimen 2 were measured at the Institute Laue Langevin, Grenoble (France) Rouquette et al. (2020); Pirling et al. (2006).

initial temperature of the base plate was at room temperature. During the deposition of the first layer, the top section of the base plate was melted what produced a strong compression force within the base plate due to the thermal expansion of the material (because of the high temperature gradient between the weld pool and the inner of the base plate).

Then the material cooled down rapidly once the welding torch moved away. During the cooling phase, the melted and heat affected zones contracted what resulted in high tensile stresses especially inside the melted zone. This behaviour is classically observed during a welding operation Coules, Colegrove, Cozzolino and Wen (2012). The successive layers produced also another similar thermal cycles but the initial temperature of the deposition surface was about 570 K to 670 K. Thus, the thermal gradient was less important especially in the ten first millimeters below the current layer. The thermal compression due to the material expansion led to a large zone of compression stresses within the base plate for 15 mm $< z <$ 45 mm. As the number of layers increased, the longitudinal stress decreased towards zero (HZB data) or to negative value (ILL data) in the last layer. Unfortunately, the neutron diffraction (ND) measurements made at the ILL did not provide reliable data within the deposits due to the small gauge volume used at the ILL (2x0.6x2 mm^3) in comparison to the one used at HZB (2x2x2 mm^3 and 10x2x2 mm^3), see table 5. The presence of large grains in the deposited zone affected the neutron diffraction signal. The bottom part of the base plate is under tensile longitudinal stresses probably due to the bending induced by the shrinkage of top base plate part. The yield stress of SS316L (as for 304L) varies from 220 MPa to 280 MPa at room temperature then drops between 150 MPa and 200 MPa at 470 K. These yield stress values have been defined experimentally by french nuclear industries: CEA, EDF and FRAMATOME Depradeux (2004). According to these values, it seems that only the melted zone and its vicinity have plasticized.

The transverse stresses are almost constant within the base plate and the deposits except for the last layer (where are the largest grains). The average transverse stress is about 10 MPa for the HZB data while this value is nearby -40 MPa for ILL data. As this average value is closer to zero, in the case of HZB measurements, it can be stated that the specimen has been loaded with an uniaxial loading (as the normal stress is also assumed to be equal to zero).

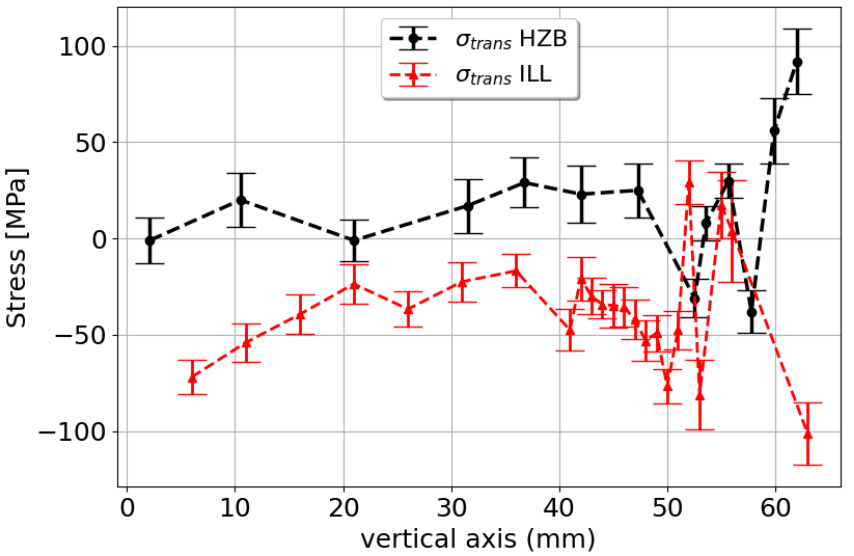

Figure 10: Transverse stress distributions along a vertical line located at x = 55 mm for two different specimens: the specimen identified HZB was built under settings 1 while the one identified as ILL was made under settings 2 (with a standard deviation of two sigma). The residual stresses in the specimen 1 were measured at Helmholtz Zentrum of Berlin (Germany) Cambon et al. (2020). The residual stresses in specimen 2 were measured at the Institute Laue Langevin, Grenoble (France) Rouquette et al. (2020); Pirling et al. (2006).

Table 6
Weld pool length in millimetre for the odd layers (layers 1, 3 and 5 respectively referred as #$L1$, #$L3$ and #$L5$) and the 3 sets of parameters (respectively referred as #$S1$, #$S2$ and #$S1$).

Layer	**Set** #$S1$	**Set** #$S2$	**Set** #$S3$
#$L1$	15.0 ± 0.4	17.6 ± 0.5	15.5 ± 0.5
#$L3$	18.5 ± 0.3	19.5 ± 0.2	19.2 ± 0.7
#$L5$	19.5 ± 0.4	21.2 ± 0.7	20.9 ± 1.0

3. Discussion: influence of process parameters

3.1. Fusion zone

The lengths of the weld pool were measured for the three different sets of process parameters. Table 6 presents the mean and standard deviation of several measurements per layer and per set of process parameters based on the images recorded during deposition. Due to the experimental set-up and the camera field, only the images of the odd-numbered layers provided the entire view of the melted zone and, thus, the length of the weld pool. There is significant scattering, both due to the dispersion caused by the measurement itself (presence of oxides on the surface of the weld pool making difficult to identify the contour of the melted zone, quantification of the number of pixels, etc...) and the process, despite its stability, can present a certain intrinsic variability. A global measurement uncertainty was estimated to ± 1 mm seemed realistic.

In general, the same trend as for the reference experiment is observed for all three types of test, i.e. an increase in the length of the melted pools with the addition of layer, even if the linear energy is the same. This is due to the competition between the heat conduction and heat losses (radiation and convection): the heat conduction slows as the initial temperature of the specimen increases with the number of layer addition Zhao, Zhang, Yin and Wu (2011); Rodrigues, Duarte, Avila, Santos, Miranda and Oliveira (2019).

The results between the three cases must be analyzed bearing the process parameters in mind (see table 1). #$S2$, which is the most energetic case (highest linear energy) led to larger weld pool sizes for all layers. The linear energy of #$S3$ is quite similar to case 1, although slightly higher. The wire feed rates of #$S2$ and #$S3$ are identical that led to an higher welding speed for #$S3$ than for #$S1$ and #$S2$ in order to maintain the orders of magnitude of the linear energy. The data in the table show that the dimensions of the weld pool of #$S2$ are between those of #$S1$ and #$S3$, which can be explained by the intermediate values of the linear energies. Nevertheless, they are very similar to those of #$S3$, which shows the importance of the wire speed parameter in the weld pool geometry as the welding current is proportional to the wire feeding.

3.2. Temperatures

Temperatures were measured at the same locations for all set of parameters investigated. Figures 11 and 12 show the values obtained for process parameter sets #$S2$ and #$S3$ respectively. The thermograms show similar trends, reflecting similar behaviors to those discussed for set #$S1$, with temperature levels varying in relation to the energy input associated with each parameter set. The specific behavior of T1 was discussed in 2.2.

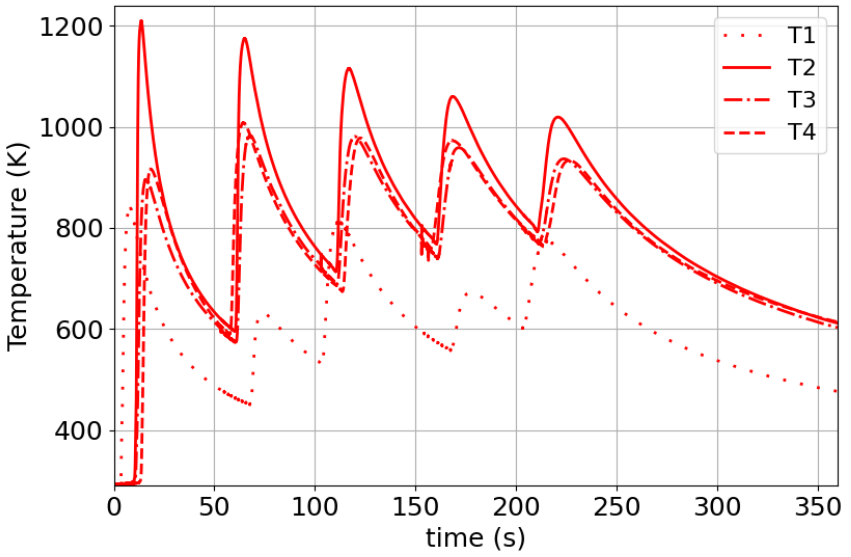

Figure 11: Thermal cycles obtained during the WAAM metal deposit and the cooling periods for #$S2$ set of parameters.

Figure 13 reports a comparison of the temperatures for the thermocouple T2 which is the closest to the deposition zone. #$S1$ and #$S3$ are very close, in relation to their respective linear energies. #$S2$, which is the most energetic case, shows clearly higher temperatures on all thermal cycles. Temperature peaks of #$S3$ occurred earlier than #$S1$ and #$S2$ as the welding speed was set to 8.6 mm/s instead of 7 mm/s for the two other cases. As the number of layers increased, this delay increased as it can be seen for the rise of temperature during the fifth layer.

3.3. Global displacement

Figure 14 shows a comparison of the free end vertical displacements for the three specimens. The three curves exhibit similar trends, with the displacement cycles corresponding to the five layers clearly identifiable.

During the final cooling, after the 5th layer has been deposited, the overall displacement of the specimens stabilized at sub-millimeter values. Whatever the studied configuration #$S1$, #$S2$ or #$S3$, the final displacements are almost identical ranging between 0.395 mm and 0.53 mm as summarized in table 7. The largest displacement is achieved with the specimen built with the highest linear energy. The specimen #$S3$ which was built with the same linear energy as specimen #$S1$ exhibited a lower vertical displacement. The faster travel speed of the welding torch likely reduced the effect of thermal expansion and thermal shrinkage between each layer. The temperature curves for specimen #$S3$ presented shorter heating and cooling cycle as the travel speed was higher, see table 1.

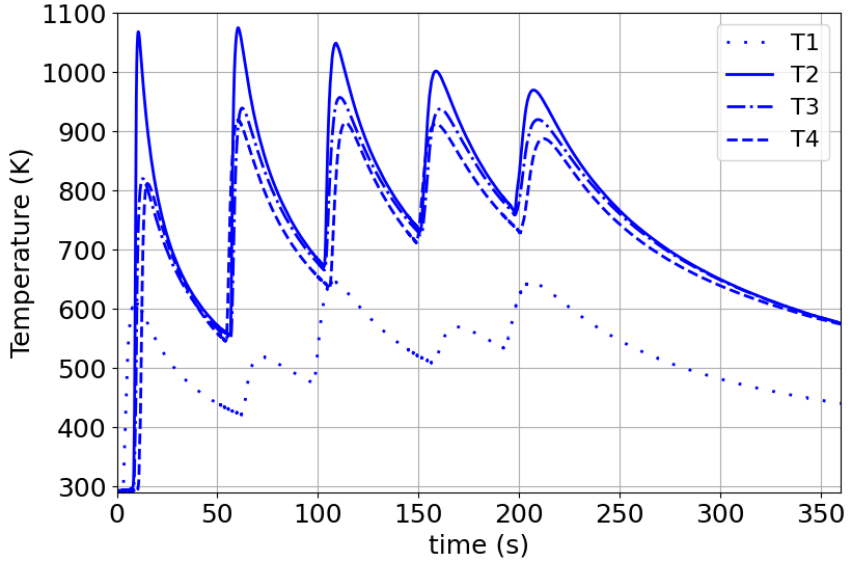

Figure 12: Thermal cycles obtained during the WAAM metal deposit and the cooling periods for #$S3$ set of parameters.

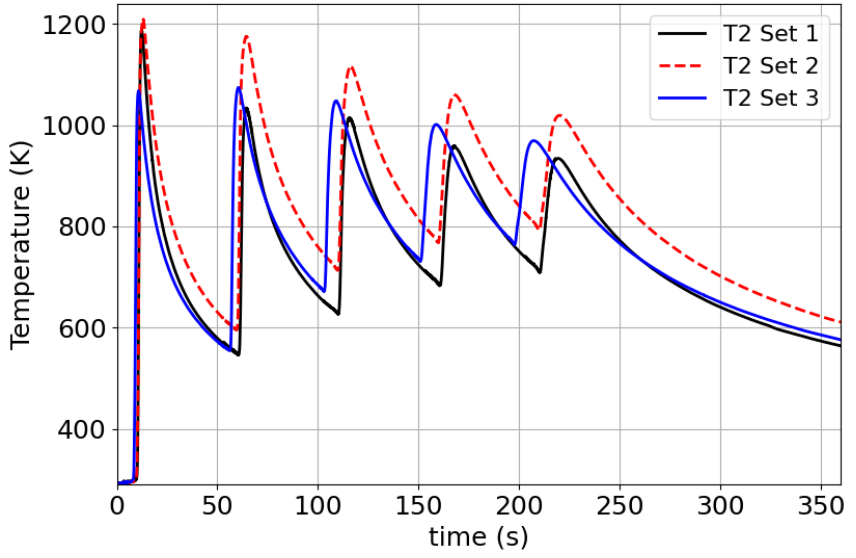

Figure 13: T2 thermal cycles for the three sets of process parameters along the deposition of 5 layers.

3.4. Residual stresses

Two different specimens have been used for neutron diffraction measurements. The longitudinal and transverse stresses are shown in figures 9 and 10. The specimen named HZB was made with set of parameter #$S1$ while the second one, named ILL, used higher linear energy (#$S2$). There is no significant difference between the two residual stress distributions measured along a vertical line as shown in 1. This vertical line is located in the thermal steady state zone. The specimen "ILL" made with set of parameters #$S2$ had a 28% higher linear welding energy than specimen "HZB" (the welding current was changed as the wire feed rate was increased). Nevertheless, the maximum and minimum stress

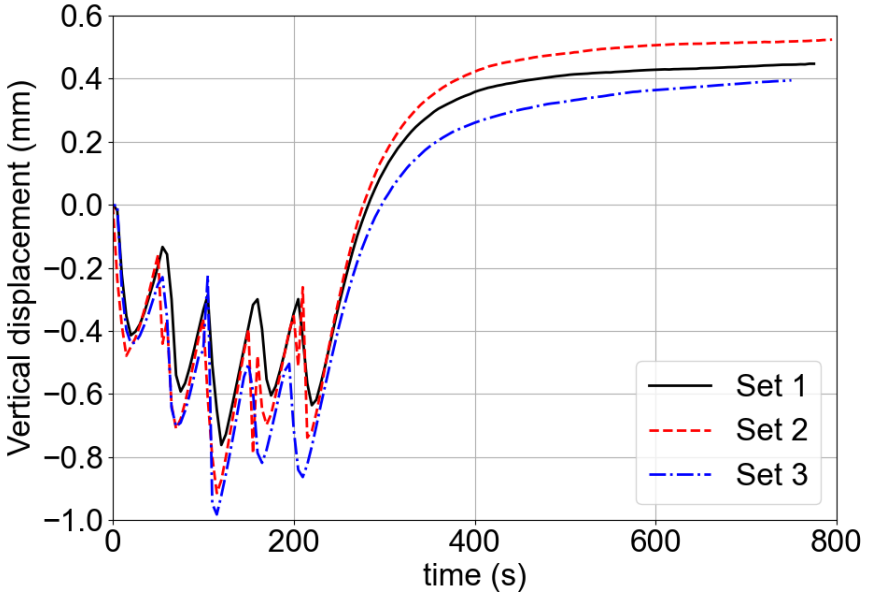

Figure 14: Vertical displacement measured during the deposit of five layers with #$S1$, #$S2$ and #$S3$ set of process parameters. The displacement is recorded with the laser displacement measuring system located at the right lower part of sample as defined by the dotted arrow in figure 1.

Table 7
Final vertical displacement of specimens built under sets #$S1$, #$S2$ and #$S3$. The uncertainty was estimated to ± 0.03 mm.

	#$S1$	#$S2$	#$S3$
Disp. (mm)	0.44	0.53	0.395

peaks are very close. The highest longitudinal stress peak is observed in the first layer for both cases with a value around 220 MPa. The minimum longitudinal stress peak is measured at 25 mm and 30 mm for "ILL" and "HZB" respectively with values of -160 MPa and -145 MPa. The base plate of each specimen was taken from the same stainless steel sheet. A slight difference in the longitudinal stress is observed in the deposited layers for specimen "ILL" where the longitudinal stress reached -70 MPa in the 5th layer in comparison to 70 MPa for specimen "HZB". Unfortunately, the volume gauge used to scan the specimen "ILL" led to poor diffracted 2θ angle, especially in the longitudinal and normal directions. The specimen sent to HZB facility was scanned with larger volume gauge, see table 5. Nevertheless, one diffracted angle, located in the last layer (z = 63 mm), was measured with a good accuracy. This unique value shows that the stress in the last layer is likely compressive. This trend must be confirmed with further neutron diffraction measurements with larger volume gage. The specimen analyzed at the HZB facility exhibits a continuous decrease of the longitudinal stress from its peak value, +220 MPa at z = 55 mm, to +80 MPa at z = 61 mm in the last layer. During the first layer, the parent is at room temperature and the yield stress for SS304L is similar to SS316L with a value of 220 MPa Depradeux (2004). As the number of layer increases, the temperature of the top part of the parent increased up to 670 K before the deposition of the 5th layer. It is well known that the yield stress value decreases with the temperature increasing. So the yield stress was lower at each new layer added what probably produced lower longitudinal stress values.

4. Conclusion

An experimental study of the impact of process parameters on WAAM specimens has been presented in this work. The study was designed as a WAAM benchmark. The experimental study was carried out in a two-dimensional way in order to work under plane stress assumption. During the manufacturing process, several data were measured in-situ: arc-voltage and welding current, temperatures with 5 thermocouples, weld pool with CCD camera and vertical displacement of the free corner of the specimen. These measurements were completed with ex-situ analysis: residual stresses were measured by neutron diffraction technique along a vertical line of a specimen. The neutron diffraction measurements have been done at two different facilities: Helmholtz Zentrum in Berlin (Germany) and Institute Laue Langevin in Grenoble (France).

The influence of process parameters, namely welding voltage, welding current and welding speed on the 3 investigated specimens can be summarized as follow:

1) The highest heating deposition were achieved with the highest linear energy as expected.
2) The longest weld pool were observed with the highest linear energy as well; nevertheless, the weld pool size increased with the number of layer added. The highest increase was observed between layer 1 and 3. The first layer was deposited on a base plate at room temperature while the next layers were deposited on warmer surface (570 K to 670 K higher) what led to larger weld pool.
3) The displacements measured during the process are linked to the contraction and expansion of the matter due to the thermal cycles (heating and cooling phases). The base plate bent downwards during the heating then upward during the cooling time. The largest distortion was observed with the specimen #$S2$ built under the highest linear welding energy (displacement of 0.52 mm). The displacement achieved with specimens #$S1$ and #$S3$ were respectively 0.44 mm and 0.39 mm.
4) The micro-structure, in the 5 deposits, is quite textured with columnar dendrite of few millimeters.
5) The effect of process parameters, so the linear energy, on the residual stress is slightly perceptible in the melted zone. Two different specimens were compared and the measured longitudinal stresses are extremely close except in the last deposited layer. The measured diffracted angles have been disturbed by the size of large grains in the fused zone. The highest longitudinal stress values were measured at the interface of base plate and first layer with values ranging between 180 MPa and 220 MPa.

This work reports a complete set of data during WAAM operation from electric signals to temperature, weld pool images and distortions recorded in-situ with ex-situ measurements: micrographic analysis and residual stresses measurements for 3 sets of process parameters. This can be useful for establishing accurate thermal-mechanical simulations of the WAAM process.

Acknowledgments

The authors are grateful for the contributions of all the participants in *Neutron Techniques Standardization for Structural Integrity European Network* (NeT) Task Group 9 on additive manufacturing and for the scientific and technical support from Sandra CABEZA of the Institut Laue-Langevin.

CRediT authorship contribution statement

Camille Cambon: Methodology, Software, Formal analysis, Investigation, Resources, Data curation, Writing original draft. **Issam Bendaoud:** Conceptualization; methodology; validation; formal analysis; investigation; ; writing review and editing. **Sébastien Rouquette:** Conceptualization; methodology; validation; formal analysis; investigation; writing review and editing. **Fabien Soulié:** Conceptualization; methodology; writing original draft preparation; supervision; project administration.

References

Abusalma, H., Eisazadeh, H., Hejripour, F., Bunn, J., Aidun, D., 2022. Parametric study of residual stress formation in wire and arc additive manufacturing. Journal of Manufacturing Processes 75, 863–876. URL: https://www.sciencedirect.com/science/article/pii/S1526612522000603, doi:https://doi.org/10.1016/j.jmapro.2022.01.043.

Akrivos, V., Wimpory, R., Hofmann, M., Stewart, B., Muransky, O., Smith, M., Bouchard, J., 2020. Neutron diffraction measurements of weld residual stresses in three-pass slot weld (Alloy 600/82) and assessment of the measurement uncertainty. Journal of Applied Crystallography 53, 1–14. doi:10.1107/s1600576720009140

Cambon, C., Rouquette, S., Bendaoud, I., Bordreuil, C., Wimpory, R., Soulié, F., 2020. Thermo-mechanical simulation of overlaid layers made with wire + arc additive manufacturing and gmaw-cold metal transfer. Welding in the World 64, 1427–1435.

Colegrove, P., Coules, H., Fairman, J., Martina, F., Kashoob, T., Mamash, H., Cozzolino, L., 2013. Microstructure and residual stress improvement in wire and arc additively manufactured parts through high-pressure rolling. Journal of Materials Processing Technology 213, 1782–1791.

Colegrove, P., Ikeagu, C., Thistlethwaite, A., Williams, S., Nagy, T., Suder, W., Steuwer, A., Pirling, T., 2009. Welding process impact on residual stress and distortion. Science and Technology of Welding and Joining 14, 717–725.

Coules, H., Colegrove, P., Cozzolino, L., Wen, S., 2012. Experimental measurement of biaxial thermal stress fields caused by arc welding. Journal of Materials Processing Technology 212, 962–968.

Depradeux, L., 2004. Simulation Numérique du Soudage – Acier 316L – Validation sur Cas Tests de Complexité Croissante (Numerical simulation of welding - Stainless Steel 316L - Validation of test cases. Ph.D. thesis. INSA Lyon.

Ding, D., Pan, Z., Cuiuri, D., Li, H., 2015. Wire-feed additive manufacturing of metal components: technologies, developments and future interests. The International Journal of Advanced Manufacturing Technology 81, 465–481.

Ding, J., Colegrove, P., Mehnen, J., Ganguly, S., Almeida, P., Wang, F., Williams, S., 2011. Thermomechanical analysis of wire and arc additive layer manufacturing process on large multi-layer parts. Computational Materials Science 50, 3315–3322.

Henckell, P., Gierth, M., Ali, Y., Reimann, J., Bergmann, J.P., 2020. Reduction of energy input in wire arc additive manufacturing (waam) with gas metal arc welding (gmaw). Materials 13, 2491–2509. doi:10.3390/ma13112491.

Honnige, J., Williams, S., Roy, J., 2017. Residual Stress Characterization and Control in the Additive Manufacture of Large Scale Metal Structures. Materials Research Forum, ICRS10 2, 455–460. doi:10.21741/9781945291173-77.

Hutchings, M., Withers, P., Holden, T., Lorentzen, T., 2005. Introduction to the Characterization of Residual Stress by Neutron Diffraction. Taylor and Francis.

Jin, W., Zhang, C., Jin, S., Tian, Y., Wellmann, D., Liu, W., 2020. Wire arc additive manufacturing of stainless steels:a review. Applied Sciences 10, 1563–1591. doi:10.3390/app10051563.

Kou, S., 2003. Welding Metallurgy. 2nd edition ed., John Wiley & Sons.

Martina, F., Roy, M.J., Szost, B.A., Terzi, S., Colegrove, P.A., Williams, S.W., Withers, P.J., Meyer, J., Hofmann, M., 2016. Residual stress of as-deposited and rolled wire +arc additive manufacturing Ti–6Al–4V components. Materials Science and Technology 32, 1439–1448. doi:10.1080/02670836.2016.1142704.

Michaleris, P., Debiccari, A., 1997. Prediction of welding distortion. Welding Journal 76.

Monier, R., Thumerel, F., Chapuis, J., Gilles, P., Soulié, F., Bordreuil, C., 2016. In situ experimental measurement of temperature field and surface tension during pulsed gmaw. Welding in the World 60, 1021–1028.

Pirling, T., Giovanni, B., Withers, P., 2006. SALSA-A new instrument for strain imaging in engineering materials and components. Materials Science and Engineering A 437, 139–144. doi:10.1016/j.msea.2006.04.083.

Poorhaydari, K., Patchett, B.M., Ivey, D.G., 2005. Estimation of cooling rate in the welding of plates with intermediate thickness. Welding Journal 84, 149–155.

Rodrigues, T.A., Duarte, V., Avila, J.A., Santos, T.G., Miranda, R., Oliveira, J., 2019. Wire and arc additive manufacturing of hsla steel: Effect of thermal cycles on microstructure and mechanical properties. Additive Manufacturing 27, 440–450. doi:https://doi.org/10.1016/j.addma.2019.03.029.

Rouquette, S., Bendaoud, I., Cabeza, S., Cambon, C., Deschaux-Beaume, F., Hacquard, C., Pirling, T., Soulié, F., 2020. Strain/stress measurement of 316L Stainless Steel additively manufactured walls with Gas Metal Arc Welding process. Technical Report. Institut Laue-Langevin (ILL). doi:10.5291/ILL-DATA.1-02-283.

Sun, J., Hensel, J., Köhler, M., Dilger, K., 2021. Residual stress in wire and arc additively manufactured aluminum components. Journal of Manufacturing Processes 65, 97–111. URL: https://www.sciencedirect.com/science/article/pii/S1526612521001079, doi:https://doi.org/10.1016/j.jmapro.2021.02.021.

Tabernero, I., Paskual, A., Álvarez, P., Suárez, A., 2018. Study on arc welding processes for high deposition rate additive manufacturing. Procedia CIRP 68, 358–362. doi:10.1016/j.procir.2017.12.095.

Wang, Z., Denlinger, E., Michaleris, P., Stoica, A.D., Ma, D., Beese, A.M., 2017. Residual stress mapping in Inconel 625 fabricated through additive manufacturing: Method for neutron diffraction measurements to validate thermomechanical model predictions. Materials and Design 113, 169–177. doi:10.1016/j.matdes.2016.10.003.

Williams, S., Martina, F., Addison, A., Ding, J., Pardal, G., Colegrove, P., 2015. Wire+arc additive manufacturing. Materials Science and Technology , 641–647doi:https://doi.org/10.1179/1743284715Y.0000000073.

Wu, Q., Mukherjee, T., De, A., DebRoy, T., 2020. Residual stresses in wire-arc additive manufacturing – hierarchy of influential variables. Additive Manufacturing 35, 101355. URL: https://www.sciencedirect.com/science/article/pii/S2214860420307272, doi:https://doi.org/10.1016/j.addma.2020.101355.

Zhao, H., Zhang, G., Yin, Z., Wu, L., 2011. A 3d dynamic analysis of thermal behavior during single-pass multi-layer weld-based rapid prototyping. Journal of Materials Processing Technology 211, 488–495. doi:https://doi.org/10.1016/j.jmatprotec.2010.11.002.